Check for updates

Controlled silanization and biomolecular conjugation *via* ultra-stable carboxyl silatrane for neurofilament light chain detection

Van-Truc Vu,[a] Pei-Yun Hsiao,[b] Ting-Chou Chang,[c] Lai-Kwan Chau [ID] *[bd] and Chun-Jen Huang [ID] *[aef]

Organofunctional silanes have garnered significant attention in materials science and nanotechnology due to their ease of use, rapid reactivity, and superior performance in adhesion, crosslinking, surface modification, moisture scavenging, and rheological enhancement. However, incorporating carboxyl functionality into alkoxysilanes remains challenging, largely due to their chemical instability arising from acid-catalyzed hydrolysis and intramolecular ring formation *via O*-acylation. In this work, we introduce an ultra-stable carboxyl silatrane (COOHSiT) engineered for controlled silanization to form thin, uniform, and functional organosilicon layers tailored for biosensor applications. The unique silatrane architecture characterized by a robust tricyclic cage and a stabilizing transannular N→Si dative bond imparts exceptional hydrolytic stability, preserving structural integrity throughout the organic synthesis and long-term storage, as confirmed by nuclear magnetic resonance (NMR) spectroscopy. Surface deposition of COOHSiT on silicon wafers was characterized using ellipsometry, contact angle goniometry, atomic force microscopy (AFM), X-ray photoelectron spectroscopy (XPS) and Fourier transform infrared (FTIR) spectroscopy. The resulting films exhibited excellent uniformity and well-controlled thickness, attributable to the precise silanization and intermolecular hydrogen bonding between amide groups. Importantly, the COOHSiT coatings maintained accessible and reactive carboxyl groups, enabling efficient downstream functionalization *via* EDC/NHS chemistry for antigen/antibody conjugation. This platform was successfully employed for neurofilament light chain (NfL) detection using a fiber-optic nanogold-linked immunosorbent assay (FONLISA), achieving an impressively low limit of detection (LOD) of 0.56 fM. Altogether, COOHSiT emerges as a highly functional and stable organosilicon building block, opening new avenues for the development of advanced functional nanomaterials and biosensing technologies.

1. Introduction

Organosilanes are a genre of monomeric silicon-derived molecules, which are widely leveraged as handy building blocks in surface/materials engineering and intermediates in organic synthesis. The biomedical industry benefits from the high biocompatibility of silane coatings for implants, medical devices and drug delivery systems.[1–5] Most of the available organosilanes have characteristics of simple handling, high reactivity, and low toxicity, offering a safe and versatile platform for a myriad of applications.[6–8] Featuring a silicon atom bonded to an organic group, typically alkyl or aryl, the silane structure is able to engage in silanization with diverse substrates *via* covalent siloxane bonds of Si–O–Si, enabling the formation of organosilicon films. Moreover, organosilanes with a broad range of terminal groups offer finely tunable interfacial properties and functionalities for numerous advanced applications, including nucleophilic substitution reactions, click chemistry, supramolecular modifications, and photochemical reactions.[5,9,10] Despite these advantages, conventional silanes are highly vulnerable to hydrolysis, followed by condensation and aggregation of disorganized silanol groups under humid

[a] Department of Chemical & Materials Engineering, National Central University, Jhong-Li, Taoyuan 320, Taiwan. E-mail: cjhuang@ncu.edu.tw

[b] Department of Chemistry and Biochemistry, National Chung Cheng University, 168 University Rd., Minhsiung, Chiayi 621301, Taiwan. E-mail: chelkc@ccu.edu.tw

[c] Instant NanoBiosensors Co., Ltd., Taipei City 115010, Taiwan

[d] Center for Nano Bio-Detection, National Chung Cheng University, 168 University Rd., Minhsiung, Chiayi 621301, Taiwan

[e] R&D Center for Membrane Technology, Chung Yuan Christian University, 200 Chung Pei Rd., Chung-Li City 32023, Taiwan

[f] School of Materials Science and Engineering, The University of New South Wales, Sydney, NSW 2052, Australia

conditions or in aqueous solvents. Additionally, the film assembly is influenced by modification conditions, including coating time and temperature, catalyst type, pH, and the water content in the solvents. As a result, achieving consistent control over molecular density, film uniformity, and reproducibility remains a significant challenge.[11–14]

Another critical limitation of commercial silane-derived products is their lack of hydrophilic functional groups, such as acids and bases, due to acid/base-catalyzed hydrolysis and ring formation *via* O-acylation.[15–17] The carboxyl group (–COOH) stands out as a highly reactive and versatile acidic functionality for many scientific and industrial communities to develop functional applications, such as ion-exchange resins, controlled drug release materials, catalysts, molecular connectors, and colloidal stabilizers.[18–24] A common strategy for biomolecular conjugation involves activating carboxyl groups to form a reactive intermediate of N-hydroxysuccinimide (NHS) ester *via* EDC (1-ethyl-3-(3-dimethylaminopropyl)carbodiimide)/ NHS coupling chemistry that can efficiently react with primary amines in target molecules.[25–27] However, introducing carboxyl groups into alkoxysilane structures is synthetically challenging, as they can readily react with the silicon center, often complicating or preventing stable compound formation.[28] Commercial carboxyl silanes are scarce and generally provided as salts in aqueous solutions, which restricts their use in organic reactions.[16] To date, only products of tri(alkoxysilyl)butanoic acid and triethoxysilylpropylmaleamic acid are commercially accessible. As previously noted, the carboxyl group can induce the hydrolysis of trialkoxysilanes owing to its acidic and hydrophilic nature. Alternatively, developing a COOH-terminated silane layer on solid substrates requires multiple surface reaction steps, leading to challenges such as increased processing complexity, longer preparation times, and potential inconsistencies in the quality and uniformity of the layer.[29,30]

Silatranes have recently attracted much attention as an advanced class of organosilicon compounds, synthesized through a simple one-step synthesis from conventional silanes.[15,31–33] Characterized by a distinctive cage-like silatranyl structure with a transannular dative bond between the silicon and nitrogen atoms in a tetrahedral arrangement, silatranes display unique chemical reactivity and exceptional stability that set them apart from traditional organosilanes. Their structural diversity arises from the ability to substitute various functional groups, leading to a plethora of derivatives with tailored properties.[31,34–36] Another notable feature of the silatrane framework is its exceptional chemical stability,[37] which renders silatranes promising candidates for applications in various fields,[35,38] including catalysis,[39] metal ion sensing and detection,[40] surface modification and adhesion promotion,[38] and antimicrobial or antifouling coatings.[15,32] These valuable characteristics highlight the multifunctionality, durability, and adaptability of silatranes – especially those bearing hydrophilic groups.[31,34,41] In previous studies, we successfully synthesized zwitterionic sulfobetaine silatrane (SBSiT) with superior hydrolytic stability compared to the counterpart of sulfobetaine silane (SBSi).[15] In addition, we developed polymerizable methacrylate silatrane

(MAST) and successfully integrated highly hydrophilic 2-methacryloyloxyethyl phosphorylcholine (MPC) with MAST to form a versatile and biofouling-resistant copolymer.[21] Silatrane compounds thus provide controllable molecular self-assemblies to generate a thin and homogeneous film with ordered molecular alignment and increased accessibility of the functional head groups towards the surroundings. As a result, the exploration of silatrane compounds continues to inspire innovation across disciplines, driving further research into their synthesis, properties, and applications in diverse fields ranging from materials science to real-world implementations.[32,38,42,43]
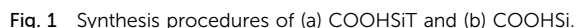
In this study, we developed an acid-functionalized carboxyl silatrane (COOHSiT) that facilitates the formation of thin, well-defined, and functionalizable organosilicon adlayers (Fig. 1(a)). These will serve as stable platforms for the construction of biointerfaces, enabling the immobilization of bio-recognition elements for molecular detection. Furthermore, the amide group in COOHSiT contributes to the facile formation of well-organized self-assembled molecules by forming intermolecular hydrogen bonds.[32,44] For comparison, we synthesized a similar carboxyl silane (COOHSi) (Fig. 1(b)) to evaluate differences in chemical stability, biocompatibility, and film-forming behavior relative to COOHSiT. Importantly, COOHSiT can be deposited on a silicon oxide surface to create a functional biointerface capable of accommodating bio-recognition elements, validated by using the enzyme-linked immunosorbent assay (ELISA). Additionally, the COOHSiT coating is able to enhance biosensing performance in a fiber optic nanogold-linked immunosorbent assay (FONLISA) for detection of neurofilament light chain (NfL), which is a promising biomarker in the context of neurodegenerative diseases (NDD) and traumatic brain injuries (TBI), as shown in Fig. 2. These outcomes highlight COOHSiT as a structurally stable and versatile organosilicon building block, offering controlled silanization to produce functional organosilicon films suitable for a wide range of applications.
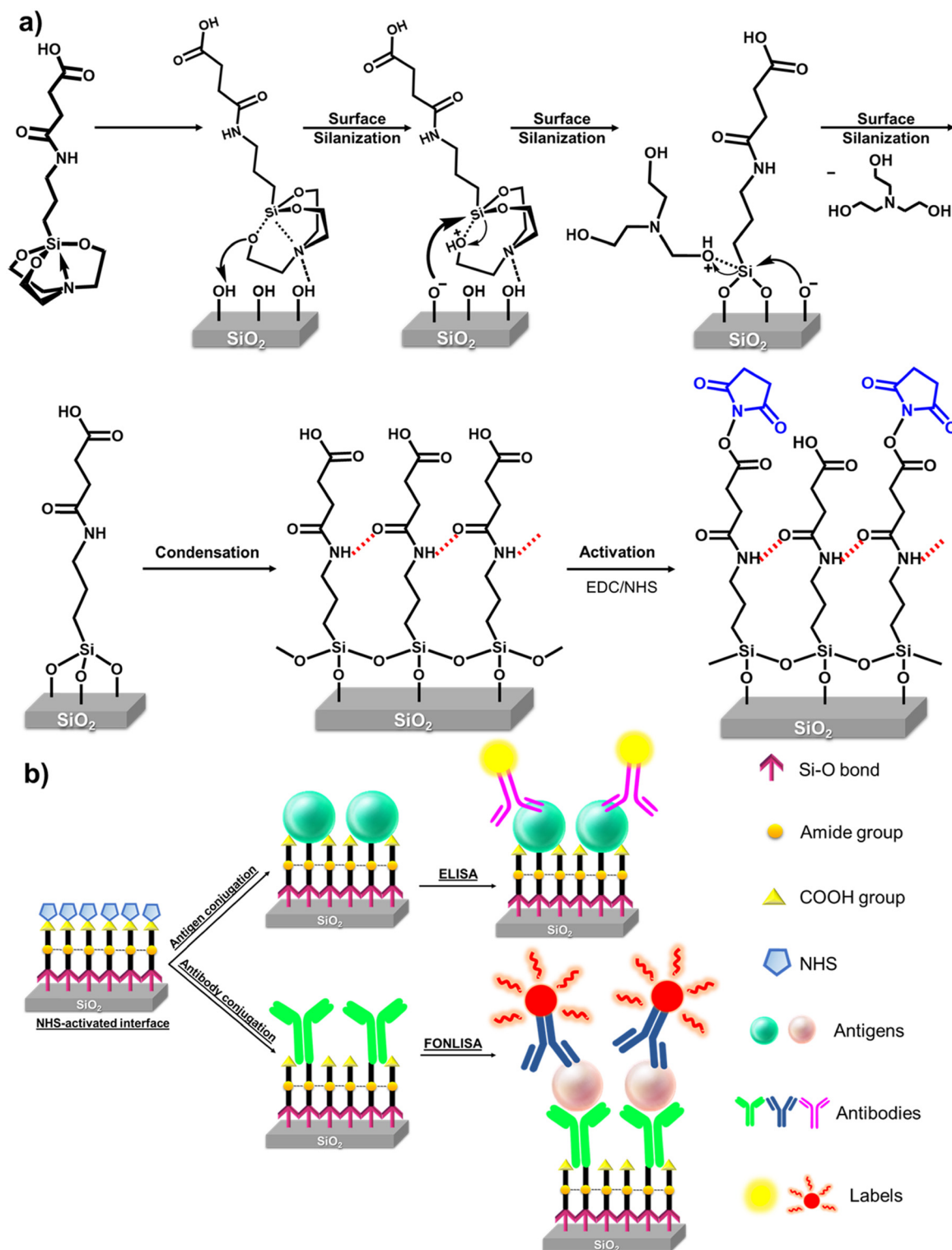
2. Experimental section

2.1 Materials

Triethanolamine (TEOA, ≥99%), succinic anhydride (SA, 99%), deuterated methanol (99.8%), trifluoroacetic acid (99%), 1,5,7-triazabicyclo[4.4.0]dec-5-ene (TBD), ethanolamine (≥98%), 16-mercaptohexadecanoic acid (16-MHDA), 2-(N-morpholino)ethanesulfonic acid (MES), bovine serum albumin (BSA), and human serum (H4522) were purchased from Sigma-Aldrich. (3-Aminopropyl)triethoxysilane (APTES, 98%) and hydrogen tetrachloroaurate were obtained from Alfa Aesar. Methanol (≥99.9%) was bought from Aencore. Acetone (≥99.8%) was sourced from ECHO, while n-pentane (≥99.9%) was obtained from Tedia. Ethanol (GC-grade, ≥99.9%) was purchased from Fisher Chemical. MEM-α (minimum essential medium α), 1-ethyl-3-(3-dimethylaminopropyl)carbodiimide (EDC, 97%), N-hydroxysuccinimide (NHS, 98%), MES buffer, and chloroform (CHCl₃, 99 + %) were obtained from Thermo Fisher Scientific. PBS

Fig. 1 Synthesis procedures of (a) COOHSiT and (b) COOHSi.

tablets were acquired from BioVision. Mouse subcutaneous connective tissue (NCTC clone 929, L-929, a derivative of Strain L) was obtained from the Bioresource Collection and Research Center (BCRC), Taiwan. Luria-Bertani (LB) agar was ordered from BD (NJ, USA). Sulfobetaine thiol (SBSH) was synthesized according to a previously reported procedure.[45] Carcinoembryonic antigen (CEA) ELISA kits were acquired from Abnova. Recombinant human neurofilament protein (ab224840) and the corresponding NfL antibody pair (ab253512) were sourced from Abcam. Ultrapure water (resistivity ≥ 18.0 MΩ cm) was produced using a ROF-50s water purification system.

2.2 Synthesis and analysis of COOHSiT and COOHSi

The synthetic routes for COOHSiT and COOHSi are illustrated in Fig. 1. For COOHSiT, 3.4 mL of APTES (14.4 mmol), 1.6 mL of TEOA (12 mmol), and 16.7 mg of TBD (0.12 mmol, used as a catalyst) were combined in a round-bottom flask under an argon atmosphere and stirred vigorously at room temperature (RT) for 30 h. The ethanol byproduct was removed *via* rotary evaporation under reduced pressure. The resulting solution was then added dropwise into 200 mL of *n*-pentane, leading to the formation of a white precipitate. This solid, identified as aminopropyl silatrane (APS), was collected by filtration and vacuum-dried with a yield of 85%. Subsequently, 1.16 g of APS (5 mmol) was dissolved in 6 mL of chloroform and added dropwise to a stirred mixture of 0.5 g of succinic anhydride (5 mmol) in 15 mL of chloroform under a nitrogen atmosphere. The system was stirred at RT for 6 h. After solvent removal *via* rotary evaporation, the crude product was washed with anhydrous acetone and vacuum-dried to yield COOHSiT as a white crystalline solid. COOHSiT was

obtained in a yield of 80% and the total yield of the two synthesis steps was 68%. The product can be stored at -20 °C as a pure solid or at 4 °C as stock solution in DMSO (0.5 M) for short-term use.

Similarly, for COOHSi, 1.17 mL of APTES (5 mmol) in 6 mL of chloroform was added dropwise to a stirred mixture of 0.5 g of succinic anhydride (5 mmol) in 15 mL of chloroform under nitrogen. The reaction proceeded at RT for 6 h. The resulting product – COOHSi – is a transparent viscous liquid which was collected after rotary evaporation and vacuum drying with a yield of 75%. COOHSi can be stored as a pure liquid at -20 °C or as stock solution in DMSO (0.5 M) at 4 °C. Techniques used for substance analyses of the newly synthesized COOHSiT and COOHSi are described in the SI.

2.3 Surface silanization with COOHSiT and COOHSi for characterization

Silicon wafers (1×1 cm^2) were cleaned by immersion in 50 mL of freshly prepared piranha solution (3 : 1 v/v concentrated H_2SO_4 to 30% H_2O_2) at 50 °C for 30 min. The wafers were then thoroughly rinsed with copious amounts of deionized water and dried under a stream of nitrogen gas. To further activate the surfaces, the wafers were treated with oxygen plasma for 15 min using a Harrick PDC-32G Basic plasma cleaner, generating hydroxyl (OH) groups on the surface. Immediately following plasma treatment, the hydroxyl-terminated wafers were immersed in coating solutions and incubated at 60 °C for 7 h. The coating solutions were prepared as follows: (1) 5 mM COOHSiT in anhydrous ethanol (COOHSiT_AE), (2) 5 mM COOHSi in anhydrous ethanol (COOHSi_AE), (3) 5 mM COOHSiT in ethanol containing 10% diH$_2$O (hydrated ethanol, COOHSiT_HE), and (4) 5 mM COOHSi in ethanol containing 10% diH$_2$O

Fig. 2 (a) Surface silanization with COOHSiT and subsequent EDC/NHS activation of COOH functional groups. (b) Further antigen/antibody conjugation *via* EDC/NHS chemistry for ELISA/FONLISA detection, respectively.

(hydrated ethanol, COOHSi_HE). After incubation, the substrates were taken out of the solutions and subjected to ultrasonic treatment in ethanol for 5 min to remove unbound molecules. The modified wafers were then dried under nitrogen stream

and further incubated at 80 °C for 2 h to promote condensation and formation of covalent Si–O–Si bonds. Surface characterization of the COOHSiT- and COOHSi-coated surfaces is described in the SI.

2.4 Activation of carboxyl groups, protein immobilization and detection by ELISA

A freshly prepared solution containing 0.2 M EDC and 0.1 M NHS in MES buffer was used to activate carboxyl-terminated surfaces. The modified silicon wafers were immersed in this EDC/NHS solution for 2 h at RT to facilitate the formation of NHS esters. Following activation, the wafers were thoroughly rinsed with deionized water, gently dried under a stream of nitrogen, and immediately subjected to subsequent characterization or protein conjugation.

CEA standard solutions, horseradish peroxidase (HRP)-conjugated anti-CEA antibodies, 3,3′,5,5′-tetramethylbenzidine (TMB) substrate, and 1 N HCl stop solution were utilized from the CEA (Human) ELISA kit. Following surface activation, each activated and non-activated COOH-terminated surface was incubated with 200 µL of CEA solution under gentle shaking for 1 h at room temperature to enable protein immobilization. After incubation, the wafers were rinsed three times with diH$_2$O and subsequently treated with 20 mM ethanolamine for 1 h to block any unreacted NHS ester groups. Next, 200 µL of goat anti-CEA HRP-conjugated antibody was applied to each surface and incubated under gentle agitation for 1 h. The wafers were then again rinsed three times with diH$_2$O. For detection, 200 µL of TMB solution was dispensed to each surface and incubated with gentle shaking for 20 min. Afterward, 100 µL of the developed TMB solution from each wafer was transferred to individual wells of a 96-well microplate. The enzymatic reaction was stopped by adding 100 µL of 1 N HCl to each well, resulting in yellow-colored solutions. Absorbance was measured at 450 nm using a microplate reader within 15 min of stopping the reaction.

2.5 Antibody immobilization and NfL detection by FONLISA

The preparation of gold nanoparticles (AuNPs) and their conjugation with the NfL detection antibody (Ab^D) were performed according to previously reported procedures[46] with minor modifications. Briefly, AuNP solutions were prepared by boiling 20 mL of an aqueous solution of HAuCl$_4$ at a concentration of 0.88 mM under a reflux system, followed by the addition of 3 mL of 1% citrate aqueous solution for 20 min until the color turned to ruby red. The mean size of the AuNPs was 12.4 ± 0.9 nm as determined by a transmission electron microscope model JEOL JEM2010. The procedures to prepare AuNP@Ab^D are as follows. 2 mL of AuNP solution with an absorbance of approximately 1.0 was mixed with 2 mL of 0.2% Tween-20 for 1 h. Then, a solution of 0.5 mM MHDA in pure water and a solution of 0.5 mM sulfobetaine thiol (SBSH) in 80% methanol were prepared and these solutions were mixed at a volume ratio of MHDA:SBSH = 1:9. Subsequently, 300 µL of the MHDA/SBSH mixture was added to the above AuNP solution and left overnight to form a mixed self-assembled monolayer (mSAM) on the AuNP surface. After centrifugation at 14 000 relative centrifugal force (rcf), the sediment was re-dispersed with deionized water to 2 mL. Then, 100 µL of a mixture containing 0.25 mM EDC and 0.43 mM NHS was added to the

reconstituted solution and allowed to react for 30 min. The excess unreacted EDC/NHS was removed by centrifugation at 12 000 rcf for 15 min and the sediment was re-dispersed with pure water to 2 mL. After activation, a solution of Ab^D was added to the reconstituted solution to yield a final concentration of 1.0 × 10^{-6} g mL^{-1}, and allowed to react for 2 h. The unreacted NHS esters on the mSAM of the AuNPs were next deactivated by adding 10 µL solution of 0.1 mM ethanolamine. Finally, the AuNP@Ab^D conjugate was collected by centrifugation at 10 000 rcf for 15 min, and the sediment was re-dispersed into pure water to have an absorbance of approximately 0.4, which corresponds to a concentration of 2 nM, for subsequent experiments.

The procedures for preparing sensor fibers and chips are as follows. The bare sensor fibers, which were 7 cm in length and consisted of optical fibers with a core diameter of 400 ± 8 µm and a buffer coating diameter of 730 ± 30 µm, featured a 2 cm partially unclad segment in the middle. These fibers were supplied by Instant NanoBiosensors Co. Ltd. To prepare a sensor fiber, firstly the bare fibers were immersed in a 1 mM ethanolic solution of COOHSiT at 60 °C for 30 min to undergo silanization, and subsequently they were placed in an oven at 110 °C for 15 min. Afterward, a silanized sensor fiber was assembled in a sensor chip following our previous procedures.[46,47] To functionalize the sensor fiber with NfL capture antibody (Ab^C), a PBS-buffered solution of Ab^C at a concentration of 1 × 10^{-5} g mL^{-1} was introduced into the sensor chip and allowed to react for 2 h. The excess activated sites on the COOHSiT layer were then deactivated by reacting with a 1 M ethanolamine solution for 7 min. Finally, a 1% BSA solution in PBS was loaded into the sensor chip and allowed to stand for 30 min. The sensor chips were then filled with 0.05% BSA in PBS to preserve for further use. For quantification of NfL standards and NfL spiked serum samples, a biosensor system previously described was employed.[46,48] In essence, the system comprised of a 530-nm light-emitting diode (LED) manufactured by Industrial Fiber Optics (model IF-E93), a sensor chip, and a photodiode (PD) produced by Hamamatsu (model S1336-18BK). The setup also incorporated a self-developed custom-built circuit board that included a current-mode driver for the LED and a photoreceiver amplification circuit to convert the current signal from the photodiode into a voltage signal. This output was then processed using a 24-bit analog-to-digital converter from National Instruments (model NI-9234) and recorded through a graphical user interface developed in LabVIEW, also by National Instruments. To perform quantitative analysis, the sensor chip was filled with a blank or a sample, to obtain the steady state transmitted light intensity I_0 or I, respectively, from the sensor fiber. The normalized intensity $(I_0 - I)/I_0$ was defined as the sensor response to establish calibration curves and compare results.

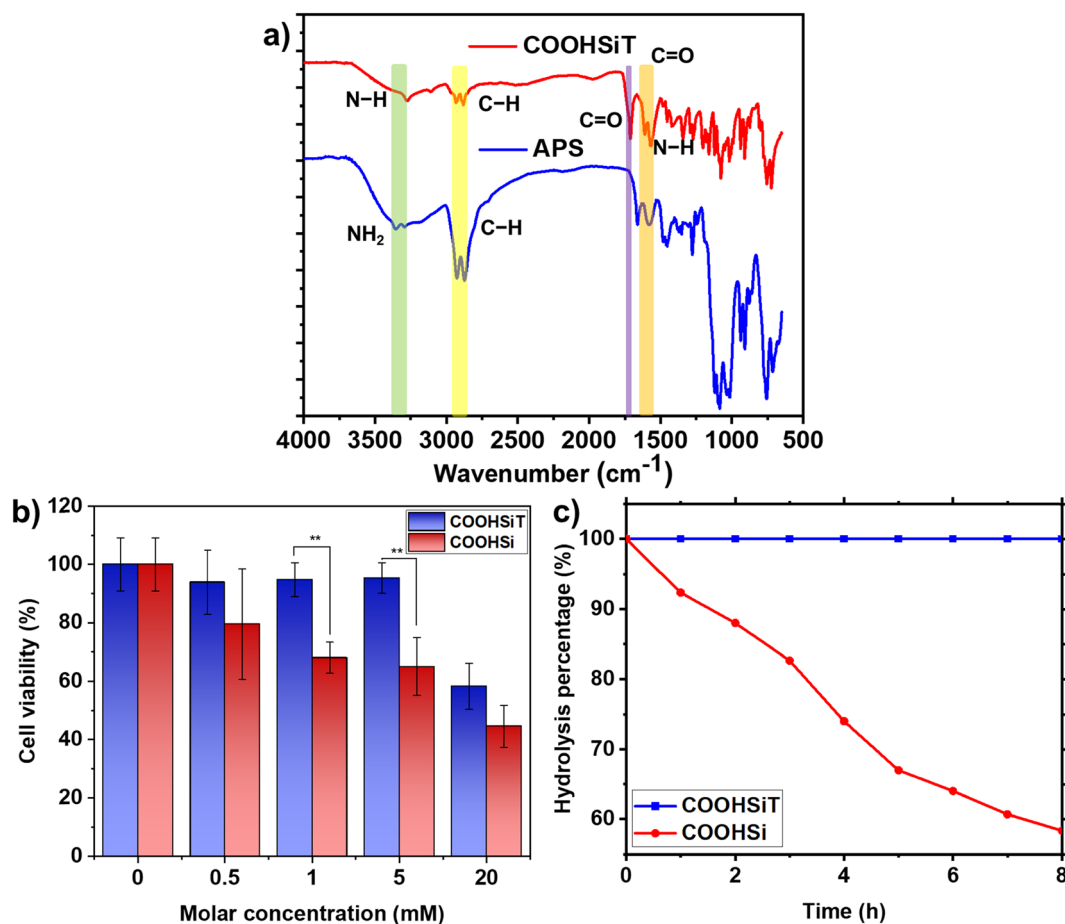## 3. Results

3.1 Substance analysis

3.1.1 Molecular structure confirmation for COOHSiT and COOHSi. The procedures for the synthesis of COOHSiT and

COOHSi are described in the Experimental section. In this synthesis process as shown in Fig. 1, succinic anhydride reacts with primary amine groups *via* a ring-opening reaction, creating an amide bond and yielding a terminal carboxylic acid. NMR spectroscopy was the first approach for elucidating the chemical structures of COOHSiT (Fig. S1) and COOHSi (Fig. S2). In the COOHSiT spectrum, two peaks that are typical of the tricyclic caged structure appear at 2.8 and 3.8 ppm.[49] On the other hand, the COOHSi spectrum reveals ethoxyl peaks at 1.2 and 3.8 ppm. The mass spectrum of COOHSiT (Fig. S3) exhibited a dominant peak at m/z = 333.1467, consistent with the calculated molecular weight of 332.43 g mol^{-1}. The observed +1 m/z shift arises from protonation of the molecule during electrospray ionization (ESI), wherein COOHSiT acquires a proton (H$^+$) from the ionization source or solvent. This results in the formation of the protonated molecular ion [M + H]$^+$, whose measured m/z value equals the molecular mass plus the proton's mass ($\approx$ 1.0078 Da). Consequently, the m/z 333.1467 peak corresponds to [M + H]$^+$ rather than the neutral molecule. To fully confirm the structure of COOHSiT, its component chemical bonds were identified by FTIR

(Fig. 3(a)). The two N–H stretching vibrations of the primary amine in APS, initially observed at 3292 and 3356 cm^{-1}, shifted to a single N–H stretching peak at 3276 cm^{-1}, which is indicative of the amide in COOHSiT. The C=O stretch of amide in COOHSiT was found at 1633 cm^{-1}, accompanied by a peak at 1566 cm^{-1} corresponding to the in-plane N–H bending of the amide group, typically found in the range of 1570 to 1515 cm^{-1}.[44] Additionally, COOHSiT presented a carbonyl (C=O) stretching band from the carboxyl group at 1711 cm^{-1}. Both APS and COOHSiT exhibited a characteristic band at 2933 cm^{-1}, attributed to C–H stretching vibrations.[50,51]

3.1.2 Biocompatibility, hydrolytic stability, and solvent compatibility of COOHSiT and COOHSi. To evaluate cytotoxicity, an MTT assay was performed using L-929 mouse fibroblast cells exposed to serial dilutions of COOHSiT and COOHSi. The L-929 cells, widely used in cytotoxicity studies, were cultured under standard mammalian cell culture conditions. The results, shown in Fig. 3(b), indicate that both compounds were non-toxic at a concentration of 0.5 mM and relatively harmful for cells at 20 mM. However, at 1 mM and 5 mM, COOHSiT exhibited higher cell viability compared to COOHSi, suggesting improved cytocompatibility.

Fig. 3 Substance analysis of COOHSiT and comparison with COOHSi. (a) Comparison of the transmittance FTIR spectra of APS and COOHSiT. (b) MTT assay for cellular viability after incubation with FBS-free DMEM containing serially diluted compounds of COOHSiT and COOHSi (n = 3, #$p \geq$ 0.05, *$p <$ 0.05, **$p <$ 0.01, ***$p <$ 0.001, ****$p <$ 0.0001). (c) Hydrolysis rate of COOHSiT and COOHSi in water-contained MeOD measured by time-course NMR.

To assess the stability of the two carboxyl-terminated organosilicons, time-course ^{1}H NMR spectroscopy was performed in methanol-d$_4$ with 10% (v/v) deionized water. Hydrolysis percentages of COOHSiT and COOHSi were calculated as shown in Fig. 3(c). Spectral changes in the signals of the silatranyl ring (δ = 2.8 and 3.8 ppm) and the ethoxy group signals (chemical shift δ = 3.8 and 1.2 ppm) were monitored over 8 hours and are shown in Fig. S4 and S5, respectively. As shown in Fig. S4, COOHSiT remained stable over time, as evidenced by two observations: the peaks belonging to the silatrane ring do not decrease in intensity, and no new peaks appear that coincide with triethanolamine – the hydrolysis product of silatrane. In contrast, for COOHSi as shown in Fig. S5, a gradual decrease in the two peaks associated with the ethoxysilane group is clearly observed, accompanied by a linear increase in the two new peaks corresponding to ethanol (chemical shift δ = 1.18 and 3.6 ppm), the hydrolysis product of the ethoxysilane group. By analyzing these changes from the initial time point, the hydrolysis rates of COOHSiT and COOHSi over time as shown in Fig. 3(c) are obtained. As presented, the silatrane ring signal remains largely unchanged, while the significant reduction in ethoxy signals indicates that COOHSi undergoes hydrolysis under aqueous conditions.

Commercial carboxylated silanes, such as carboxyethylsilanetriol disodium (CES) and N-(trimethoxysilylpropyl)ethylenediamine triacetic acid trisodium salt (TMS-EDTA), are supplied as salts in aqueous solutions. This limits their potential for widespread application, especially in organic solvents.[16] To assess solvent compatibility, the solubility of COOHSiT and COOHSi was tested in various organic solvents at concentrations of 0.1 g mL^{-1} and 0.01 g mL^{-1} at room temperature. Solubility was categorized as "soluble" ($\geq$1 g/10 mL), "slightly soluble" (0.1–1 g/10 mL), or "insoluble" (<0.1 g/10 mL), as summarized in Table S1. Both compounds contain a polar carboxyl group, so they dissolved easily in highly polar solvents like water, DMF, and DMSO. Solubility decreased with decreasing solvent polarity. Minor differences in solubility between COOHSiT and COOHSi were observed in alcohols.

3.2 Coating characterization

3.2.1 Thickness and hydrophilicity of COOHSiT and COOHSi coatings.
The deposition of COOHSiT and COOHSi on silicon wafers to form organosilicon thin films was characterized. Coatings were prepared in anhydrous ethanol (AE) and hydrated ethanol (HE) containing 10% (v/v) deionized water. As presented in Fig. 4(a), the thicknesses of COOHSiT_AE and COOHSi_AE films were 2.7 ± 0.2 nm and 6.1 ± 1.3 nm, respectively. In contrast, COOHSiT_HE and COOHSi_HE films were thicker, measuring 4.1 ± 0.1 nm and 23.4 ± 3.2 nm, respectively. Under both solvent conditions, silatrane-based films were consistently thinner than their silane counterparts. The hydrophilicity of the carboxyl-functionalized surfaces is reflected *via* water contact angle (WCA) in Fig. 4(b). COOHSiT_AE and COOHSiT_HE coatings had similar WCAs, indicating that water content during the coating process had a marginal effect on their surface wettability. In contrast, the COOHSi coatings exhibited notable differences, with COOHSi_AE coatings displaying a WCA of 21.7° ± 0.8°, whereas COOHSi_HE coatings showed a significantly higher WCA of 57.9° ± 1.3°.

3.2.2 Morphology and roughness of COOHSiT and COOHSi coatings.
Atomic force microscopy (AFM) was employed to investigate the surface topography and roughness of both bare and silanized substrates, as presented in Fig. 5(a)–(f). Among the modified surfaces, COOHSiT coatings prepared in anhydrous ethanol (Fig. 5(a)) exhibited the most uniform and homogeneous morphology, characterized by shallow and evenly distributed corrugations. Similarly, COOHSiT surfaces formed in hydrated ethanol (Fig. 5(b)) displayed a comparable, though slightly rougher, profile featuring uniformly dispersed small humps and agglomerates. In contrast, COOHSi coatings prepared in anhydrous ethanol (Fig. 5(c)) exhibited increased surface roughness, an effect that was further pronounced in the COOHSi coatings deposited in hydrated ethanol (Fig. 5(d)), which revealed the presence of large clustered features contributing to significant surface heterogeneity. The bare silicon substrate (Fig. 5(e)) appeared smooth and featureless, with the lowest root mean square (RMS) roughness value of 0.14 ± 0.09 nm.
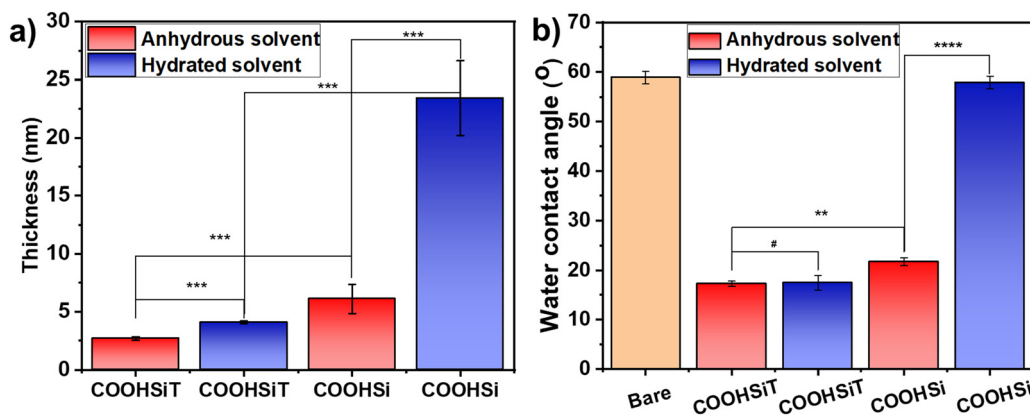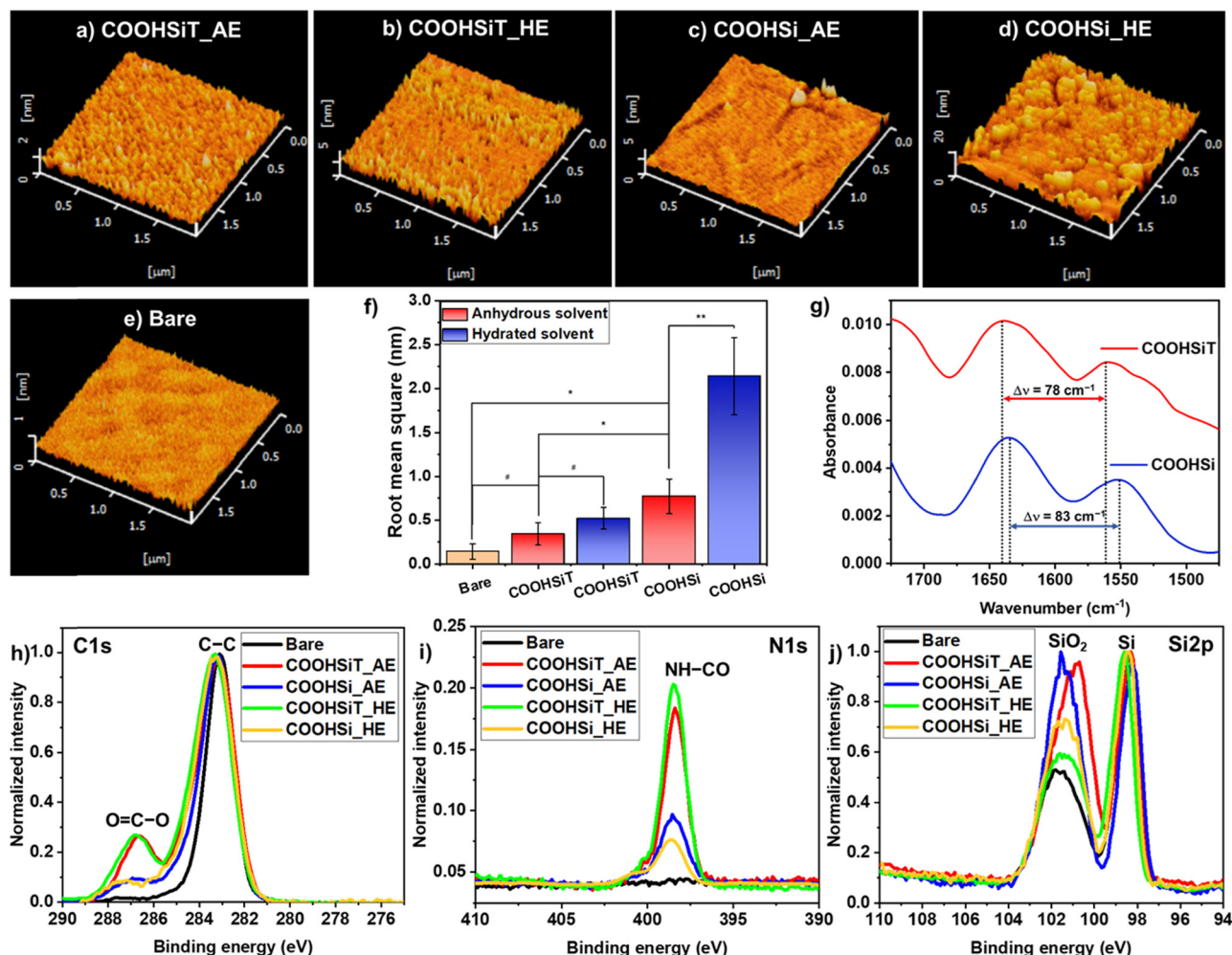

Fig. 4 (a) Contact angle and (b) thickness measurements for COOHSiT and COOHSi films coated in anhydrous ethanol and hydrated ethanol (ethanol containing 10% diH$_2$O) (n = 3, #p $\geq$ 0.05, *p < 0.05, **p < 0.01, ***p < 0.001, ****p < 0.0001).

Fig. 5 Surface characterization of COOHSiT- and COOHSi-coated substrates. AFM profiles of (a) COOHSiT-coated surfaces in anhydrous ethanol (COOHSiT_AE), (b) COOHSiT-coated surfaces in hydrated ethanol (COOHSiT_HE), (c) COOHSi-coated surfaces in anhydrous ethanol (COOHSi_AE), (d) COOHSi-coated surfaces in hydrated ethanol (COOHSi_HE), and (e) bare surface (the vertical axis refers to z-scale, which represents the height of measured topography). (f) RMS values of tested surfaces ($n = 3$, #$p \geq 0.05$, *$p < 0.05$, **$p < 0.01$, ***$p < 0.001$, ****$p < 0.0001$). (g) IR spectra in the 1725–1475 cm^{-1} spectral range of COOHSiT- and COOHSi-coated wafers. XPS spectra of (h) C 1s, (i) N 1s and (j) Si 2p for the COOHSiT- and COOHSi-modified Si wafers.

Quantitative analysis of RMS values across all surfaces (Fig. 5(f)) confirmed that COOHSiT_AE coatings had the lowest roughness among the functionalized samples (0.34 ± 0.13 nm), whereas COOHSi_HE surfaces displayed the highest roughness due to the formation of large surface clusters. Intermediate RMS values were observed for COOHSiT_HE and COOHSi_AE surfaces, consistent with their moderately corrugated morphologies.

3.2.3 Intermolecular hydrogen bonding of COOHSiT and COOHSi layers. FTIR with specular reflection was employed to further analyze the COOHSiT and COOHSi coatings prepared in anhydrous ethanol. The IR spectra of the COOH-terminated monolayers are presented in Fig. 5(g), covering the range from 1700 to 1400 cm^{-1}, which corresponds to the characteristic amide I and amide II regions.[44] In the COOHSiT spectrum, two broad peaks were observed at 1638 and 1560 cm^{-1}, attributed to the amide I ($\nu_{C=O}$) and amide II ($\delta_{NH} + \nu_{C-N}$) bands, respectively. Similarly, the COOHSi spectrum exhibited the corresponding peaks at 1635 and 1552 cm^{-1}. These wide bands verify that both COOHSiT and COOHSi are successfully grafted onto the surfaces, while the wavenumber difference ($\Delta\nu$) between the amide I and amide II bands of each SAM indicates the existence of intermolecular hydrogen bonds.[44] In this work, $\Delta\nu$ was calculated as 78 cm^{-1} for the COOHSiT film and 83 cm^{-1} for the COOHSi film.

3.2.4 Elemental composition and chemical state of COOH-SiT and COOHSi coatings. High-resolution XPS was used to analyze the elemental composition and chemical states of bare and modified silicon substrates (Fig. 5(h)–(j)). In the C 1s spectra, all signals were normalized to the highest intensity of the C–Si/C–C peak at 283.2 ± 0.2 eV.[52,53] Carbon on bare silicon wafers typically appeared as an impurity or residue from processing.[54] In coated samples, the C 1s peak broadened toward higher binding energies, with a characteristic C–C bond peak at 284.6 ± 0.2 eV.[55,56] The peaks at 287.3 ± 0.2 eV
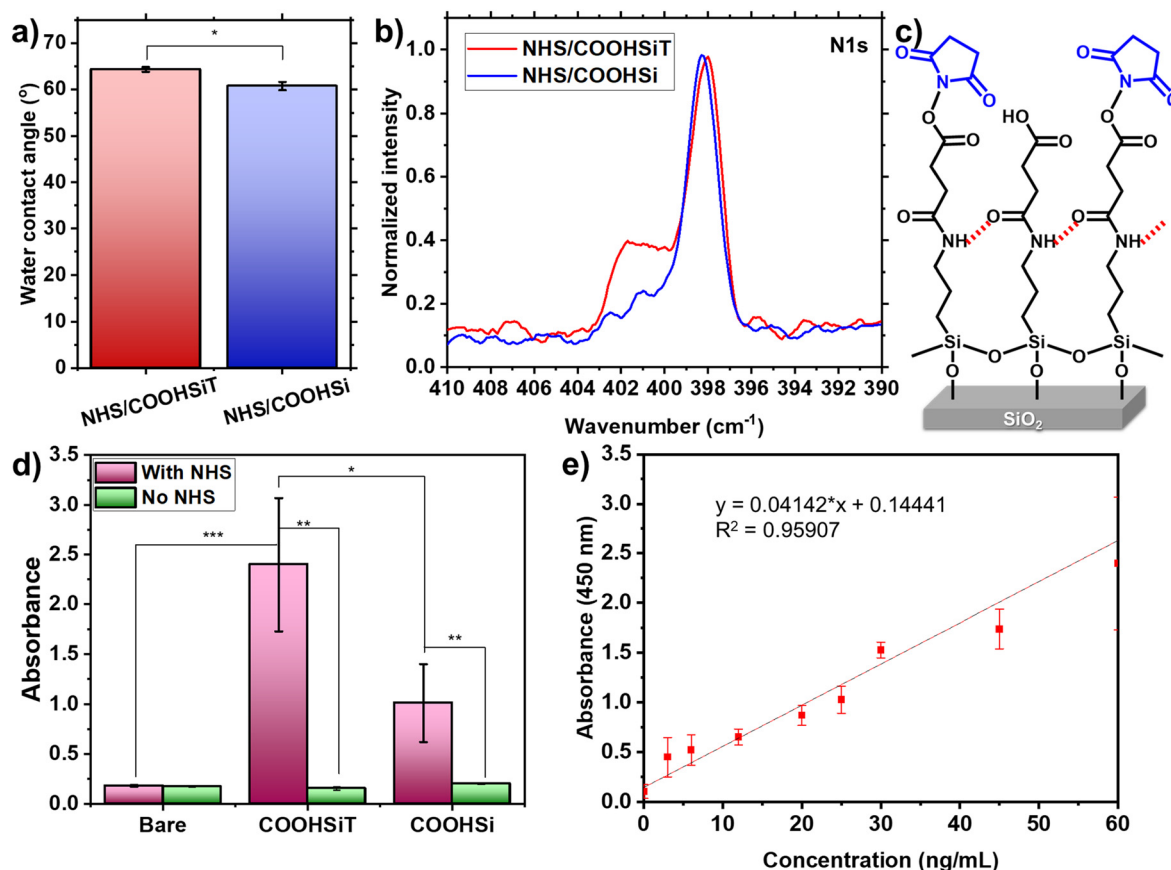
corresponded to C=O bonds in amide and carboxyl groups, confirming deposition of COOHSiT and COOHSi. As shown in Fig. S6, additional deconvolution showed the peaks at 286.6 eV and 288.2 eV which were attributed to O=C–N and O=C–O groups, respectively, with nearly equal peak areas reflecting the expected 1 : 1 ratio.[53–57] Water content in coating solutions had minimal impact on the normalized intensities of both COOH-SiT and COOHSi layers. In the N 1s spectra, intensities were normalized to the maximum C 1s signal for each sample. The nearly flat signal at the bare surface reflects a negligible presence of elemental N. A peak at 398.5 eV was observed for all silanized coatings, indicating amide group formation.[58]

In the Si 2p spectra, the crystalline Si[0] peak was used to normalize signals from amorphous silyl (Si–C), silicon oxide (SiO₂), silanol (Si–OH), and siloxane (Si–O–Si) bonds.[59,60] The modified surfaces afforded higher normalized intensities of Si oxide than the bare wafer, consistent with the addition Si–O–Si bonds between the molecules and to the surface. As shown in Fig. S7, the Si–O signal exhibited consistently higher intensity than the Si–C signal, which is consistent with the presence of various interfacial species such as silicon oxide, silanol, and siloxane, as previously reported. Notably, the COOHSiT

coatings prepared in anhydrous ethanol (COOHSiT_AE) displayed a higher relative content of Si–O species compared to those formed in hydrated ethanol (COOHSiT_HE), despite exhibiting comparable film thickness. This observation suggests that the COOHSiT_AE surfaces have a higher molecular packing density or more extensively reacted silane units per unit area, resulting in a more pronounced Si–O signature in the XPS spectra.

3.3 Activation and bioconjugation of COOH-terminated interfaces

3.3.1 NHS-activation for COOH-terminated interfaces. The accessibility to carboxyl groups on COOHSiT and COOHSi coatings prepared in anhydrous ethanol was evaluated *via* EDC/NHS activation, as described in Fig. 2. WCA measurements and XPS were used to assess the efficiency of NHS coupling (Fig. 6(a)–(c)). Following activation, WCA values increased significantly to $64.3° \pm 0.5°$ for NHS/COOHSiT and $60.7° \pm 0.9°$ for NHS/COOHSi. Notably, the NHS/COOHSiT films exhibited a more pronounced increase in WCA, despite originating from a lower initial value, as shown in Fig. 4(b). XPS analysis further confirmed successful NHS activation, as

Fig. 6 Activation and application of COOH-terminated coatings. (a) WCAs and (b) XPS N 1s spectrum of COOHSiT- and COOHSi-coated wafers after EDC/NHS activation ($n = 3$, #$p \geq 0.05$, *$p < 0.05$, **$p < 0.01$, ***$p < 0.001$, ****$p < 0.0001$). (c) Schematic illustration of the COOH-terminated surface after activation with NHS. (d) ELISA absorbance values reflect CEA immobilization on bare and COOH-terminated surfaces with and without EDC/NHS activation ($n = 3$, #$p \geq 0.05$, *$p < 0.05$, **$p < 0.01$, ***$p < 0.001$, ****$p < 0.0001$). (e) Plot of ELISA absorbance on COOHSiT films *versus* applied CEA concentration *via* EDC/NHS coupling for immobilization.
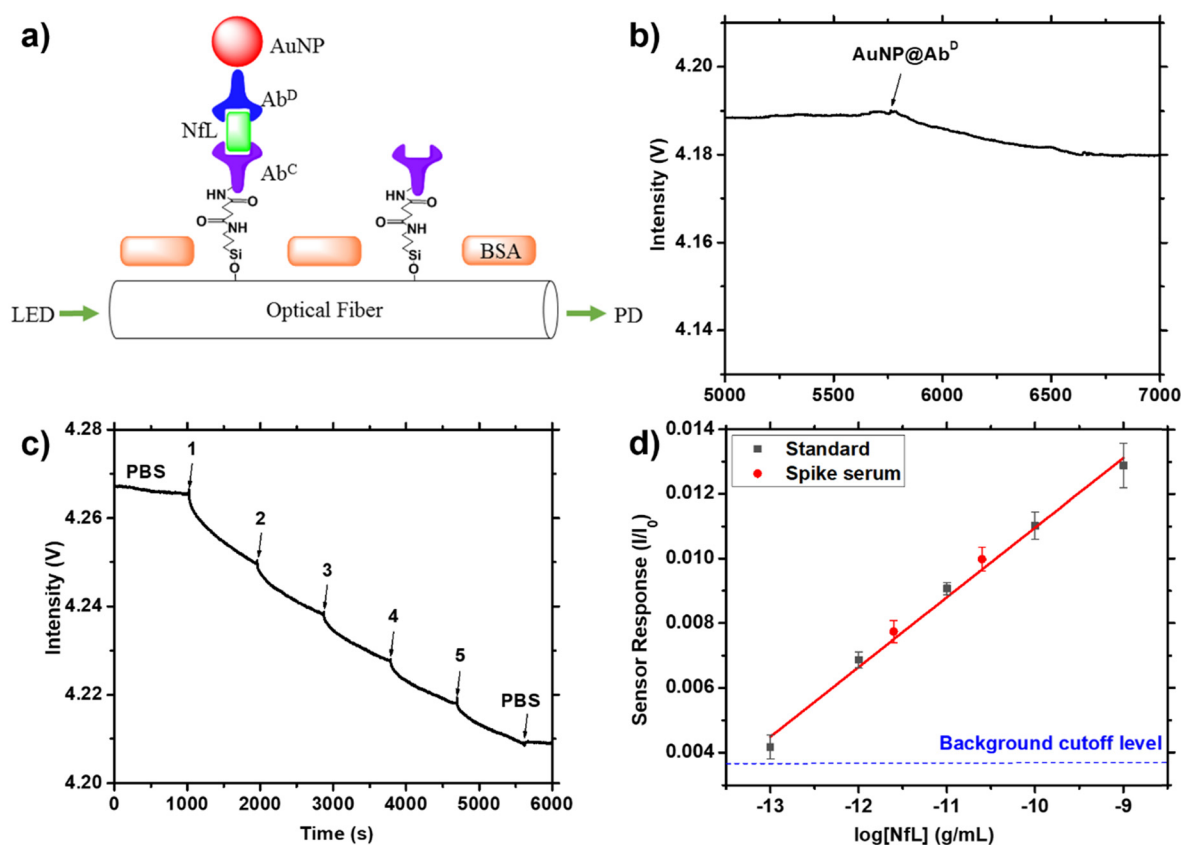
indicated by the emergence of a new N 1s peak at 401.6–401.8 eV in both films, corresponding to the *N*-hydroxysuccinimide ester (–COO–N–C$_2$). This peak was significantly more prominent in the COOHSiT films, with an integrated area approximately 2.5 times larger than that observed in the corresponding COOHSi films (Fig. S8).

3.3.2 Protein conjugation on COOH-terminated interfaces and detection by ELISA. To evaluate protein immobilization on activated COOH-terminated films, carcinoembryonic antigen (CEA) – a glycoprotein associated with multiple cancers[61] – was employed. The specific procedure was based on ELISA. As shown in Fig. 6(d), significantly higher levels of CEA immobilization were observed on NHS-activated surfaces compared to bare or non-activated ones. Among the activated films, the COOHSiT coatings captured more CEA than the COOHSi coatings, as evidenced by a stronger detection signal. This result aligns with previous findings, indicating more efficient COOH activation on COOHSiT surfaces. Further testing with varying CEA concentrations on NHS-activated COOHSiT surfaces demonstrated a concentration-dependent increase in ELISA absorbance (Fig. 6(e)), confirming the effective accommodation of bio-recognition elements.

3.3.3 FONLISA method based on an antibody-conjugated COOH-terminated interface for detection of neurofilament light chain (NfL). The FONLISA method is a sandwich-type detection platform. In this approach, a capture antibody (Ab^C) is immobilized on the optical fiber core surface, while a detection antibody (Ab^D) is conjugated to a gold nanoparticle (AuNP) to form an AuNP@Ab^D conjugate. The target antigen (A) is detected by forming a sandwich complex, AuNP@Ab^D–A–Ab^C, on the sensor surface, as illustrated in Fig. 7(a). In the FONLISA method, the background nonspecific adsorption (BNA) of AuNP@Ab^D on the fiber core surface impacts the limit of detection (LOD). Therefore, BNA tests were conducted to evaluate how effectively the COOHSiT layer, after BSA blocking, resists nonspecific adsorption of AuNP@Ab^D on the sensor surface. The BNA tests were performed by loading an AuNP@Ab^D solution into an Ab^C-functionalized sensor chip in the absence of NfL. A typical sensorgram is shown in Fig. 7(b); the sensor response ($\Delta I/I_0$) was 0.00177 ± 0.00064 (n = 4). To eliminate false positive signals caused by BNA, we defined a background cutoff level (B) as the mean sensor response from BNA plus three times its standard deviation. Based on this definition, the B value was determined to be 0.00367, corresponding to a 99.7% confidence level.

The feasibility of using the COOHSiT layer as an interface for a biosensor in a sandwich format is illustrated by a

Fig. 7 (a) Schematic representation of the FONLISA method; (b) sensorgram obtained upon injection of a AuNP@Ab^D solution in the absence of NfL; (c) sensorgram in response to serial injection of NfL standards with a concentration of (1) 1.0×10^{-13}, (2) 1.0×10^{-12}, (3) 1.0×10^{-11}, (4) 1.0×10^{-10}, and (5) 1.0×10^{-9} g mL^{-1} at a fixed concentration of AuNP@Ab^D; (d) calibration curve for NfL detection using NfL standards (black squares) and sensor responses for NfL spiked serum samples (red circles). The linear regression line is shown in red color and the background cutoff level is shown as a blue dashed line.

representative sensorgram (Fig. 7(c)) under sequential injection of NfL standards with increasing concentration into an Ab^C-functionalized sensor chip. The NfL standards consisted of PBS solutions containing a fixed concentration of AuNP@Ab^D and varying concentrations of NfL from 1.0×10^{-13} to 1.0×10^{-9} g mL^{-1}. The flow of each sample was stopped when the microchannel was completely occupied by the injected sample, and each injection lasted 15 min to reach steady state. The standard calibration curve, as depicted in Fig. 7(d), was established by plotting the sensor response *versus* the logarithm of each NfL concentration. The linear regression equation derived from the calibration curve is $y = 0.00222x + 0.03343$, where $x =$ log[NfL] (g mL^{-1}) ($r^2 = 0.992$). The calibration curve manifests a wide linear dynamic range of 4 orders of magnitude, from 1.0×10^{-13} to 1.0×10^{-9} g mL^{-1}. The method using the COOHSiT interface is highly reproducible, with coefficients of variation (CV) for these data points below 8.8%. Using the B value as the minimum distinguishable analytical signal, the LOD is calculated to be 3.9×10^{-14} g mL^{-1}, corresponding to 0.56 fM. Compared with our previous immunoassays using the FONLISA method,[46,48] this LOD is remarkably low, highlighting the superior performance of the COOHSiT interface for immunoassay development.

To evaluate the analytical performance of the COOHSiT interface in the presence of matrix effects, two NfL spiked serum samples were tested. As shown in Fig. 7(d), the sensor responses of the two spiked samples aligned well with the calibration curve, yielding recoveries of 109.4% and 106.9% for NfL concentrations of 2.5×10^{-12} and 2.5×10^{-11} g mL^{-1}, respectively. These favorable recoveries indicate that the COOHSiT interface provides excellent surface properties, enabling high selectivity in complex human serum matrices.

4. Discussion

4.1 Development of COOHSiT/COOHSi and controlled silanization

The successful synthesis and structural identities of COOHSiT and COOHSi are supported by multiple analytical techniques. The proton NMR spectrum of COOHSiT confirms the presence of the tricyclic caged silatrane structure.[15,32,33,49] Meanwhile, COOHSi displays ethoxy peaks characteristic of the original APTES precursor. The remaining peaks in the NMR spectra of both compounds are similar, reflecting their shared structural features. Mass spectrometry data provide additional confirmation of the proposed molecular structure of COOHSiT. FTIR spectroscopy further confirms the presence of the expected functional groups. Collectively, these spectral findings validate the successful development of COOHSiT and COOHSi.

Silatranes have been proved to exhibit superior resistance to hydrolysis compared to conventional silanes.[15,32,33] The enhanced stability of silatranes arises from their cage-like structure, which shields the central silicon atom and reduces its reactivity through a strong intramolecular Si ← N dative bond. Hydrolyzing COOHSiT thus requires breaking this bond

and disrupting the cage edges, making the process energetically demanding.[31,34] Conversely, the silicon center in COOHSi is more exposed, facilitating nucleophilic attack by water and acid-catalyzed hydrolysis (Fig. 8(a)). The hydrolytic instability of silanes is associated with their susceptibility to hydrolysis by water, which is further facilitated by carboxylic acid (–COOH) groups. The hydrolysis of silanes in water-containing environments has been extensively discussed in previous studies, particularly in relation to alkoxy-functional silanes, which readily react with water.[12,13,62] Briefly, the –Si–OR (alkoxy) groups undergo nucleophilic substitution with water, forming silanol groups (–Si–OH) and releasing alcohol (R–OH). These silanol groups can subsequently condense with other silanols to create siloxane networks (Si–O–Si). In this study, we further discovered that the presence of an acid functional group promotes this process to occur faster (within hours), compared to silane with a hydrophobic methacrylate functional group studied previously (several days).[32] This mechanism involves the ability of the acid group to donate protons, thus catalyzing the breakdown of Si–OR bonds – similar to general acid catalysis.

Moreover, COOHSiT and COOHSi demonstrate broader solubility profiles compared to commercial carboxylated silanes like CES and TMS-EDTA, which are poorly suited for use in organic solvents.[16] The neutral molecular structures and polar functional groups of COOHSiT and COOHSi enhance their compatibility with a variety of polar solvents. According to the "like dissolves like" principle,[63,64] their solubility in solvents such as water, alcohols, and DMF is facilitated by hydrogen bonding and dipole–dipole interactions. The slightly lower solubility of the silane derivative compared to its silatrane analogue can be explained by the greater tendency of the triethoxysilyl group to undergo partial hydrolysis and self-condensation, promoting aggregation.[15,32] In addition, the intramolecularly coordinated nitrogen atom in silatrane increases molecular polarity and allows weak interactions with alcohol solvents, resulting in improved solubility.[31,34]

As safety is paramount, the cytotoxicity of the two new organosilanes warrants evaluation. The stable Si ← N dative bond of COOHSiT reduces its reactivity and slows hydrolysis, thereby limiting the release of potentially harmful by-products.[31,34] In contrast, COOHSi hydrolyzes more readily, producing ethanol and silanol (Si–OH), which are associated with cytotoxic effects.[65–68] This property suggests a potential advantage of COOHSiT in biological and environmentally sensitive applications.

4.2 Comparative deposition of COOHSiT and COOHSi under hydrated and anhydrous conditions

The increased film thickness observed when using hydrated solvents is attributed to hydrolysis-driven condensation and molecular aggregation during deposition. This effect is particularly pronounced for COOHSi, which exhibits a significant increase in thickness in hydrated solvents – likely resulting from partial hydrolysis (>40%) of ethoxy groups after 8 h (Fig. 3(c)). This promotes rapid crosslinking and aggregation in solution and on the surface.[17,32,33] In contrast, the silatrane
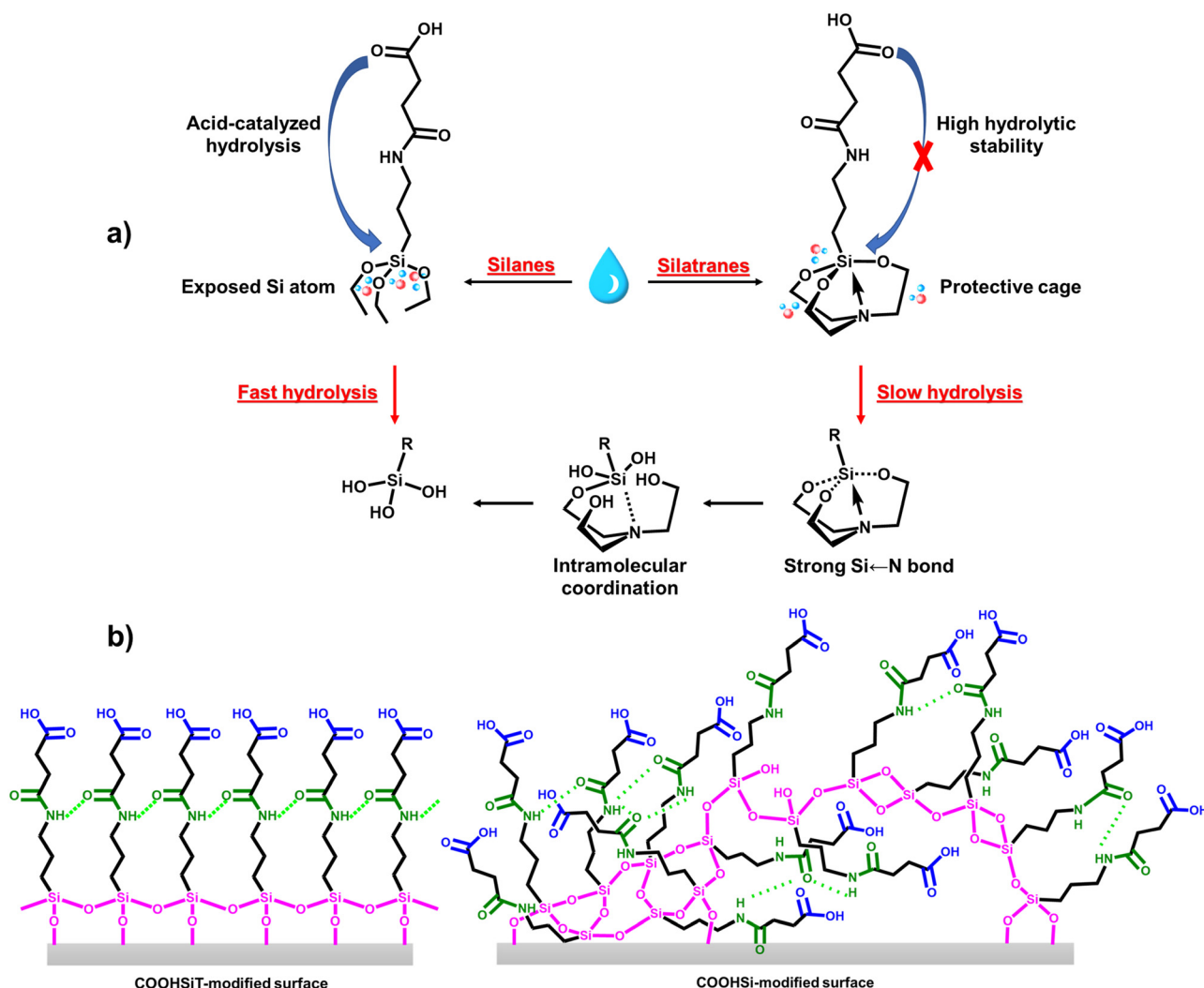
Fig. 8 Schematic illustration of (a) the hydrolysis of silatranes *versus* silanes and (b) molecular organization in COOHSiT- and COOHSi-coated surfaces.

structure of COOHSiT limits hydrolysis and aggregation, resulting in thinner, more controlled coatings as indicated by the AFM results (Fig. 5(a)–(f)). WCA measurements further highlight surface differences. Most coatings, with the exception of COOHSi_HE, exhibit WCA values characteristic of carboxyl-terminated surfaces.[69] The sharp WCA increase in COOHSi_HE and COOHSi_AE suggests enhanced porosity and air trapping, which leads to increased hydrophobicity.[70] In contrast, COOHSiT films maintain consistently low WCA values. Moreover, FTIR vibrational analysis further confirms stronger intermolecular hydrogen bonding in COOHSiT films, indicated by smaller $\Delta\nu$ values – suggesting a denser and more ordered molecular arrangement.[44,71,72]

XPS C 1s and N 1s spectra confirmed amide and carboxyl groups on both COOHSiT- and COOHSi-coated surfaces. The absence of a tertiary amine peak (400–402 eV) confirmed effective TEOA removal. Si 2p spectra showed lower normalized Si–O intensities for AE-derived coatings, which aligns with their thinner profiles. The thickest COOHSi_HE coatings exhibited a higher Si–O signal but a lower signal for COOH groups,

reflecting thick and irregular deposition of organosilicons, which is consistent with the findings from ellipsometry, AFM and contact angle measurements.

Overall, COOHSiT coatings consistently outperformed COOHSi in all key surface properties. The performance of COOHSi, especially from hydrated ethanol, reflects water-driven hydrolysis and uncontrolled aggregation, resulting in increased thickness, reduced hydrophilicity, and higher roughness. In contrast, COOHSiT enables controlled silanization, producing thin, smooth, uniform films with high molecular density, orderly packing, and accessible functional groups. Hydrated solvents had only a minor negative effect on COOHSiT, slightly increasing thickness and modestly reducing hydrophilicity and smoothness. By comparison, hydrated solvents severely degraded COOHSi film quality through enhanced aggregation and poorer surface uniformity. Silatranes exhibit distinct surface-binding behavior compared to conventional trialkoxy-silanes due to their unique intramolecularly coordinated sila-trane cage structure. In silatranes, the N→Si dative bond stabilizes the silicon center, reducing its electrophilicity and

thereby slowing the rate of hydrolysis and condensation reactions that lead to siloxane network formation. This controlled reactivity minimizes premature polymerization in solution and allows more uniform surface attachment during deposition. Upon hydrolysis, the silatrane framework gradually releases the active silanol species in a self-regulated manner, promoting dense, well-ordered monolayer formation with strong Si–O–substrate bonds.[31,34,73] Consequently, silatranes provide enhanced stability, reproducibility, and control in surface functionalization compared to conventional silane coupling agents. The proposed molecular arrangement (Fig. 8(b)) underscores the superior structural and functional advantages of silatrane-based coatings, making them ideal for applications requiring precise and robust surface engineering.

4.3 Functionalization and applications of COOH-terminated coatings

COOHSiT facilitates superior immobilization of bio-recognition elements *via* EDC/NHS coupling, attributed to its higher molecular density and accessible functional groups. The correlation between protein concentration and biosensor signal further demonstrated excellent sensitivity and discrimination capability of the COOHSiT functional interface. In the FONLISA method, the COOHSiT interface enabled highly sensitive and reproducible NfL detection, with a wide linear range, excellent linearity, and a low LOD of 0.56 fM. Additionally, successful recovery in NfL-spiked serum samples (109.4% and 106.9%) confirmed high selectivity and robustness of the COOHSiT interface against matrix effects. Overall, these findings underscore the advantages of silatrane-based COOHSiT coatings in biointerfaces, offering enhanced molecular organization, higher coupling efficiency, and greater protein-loading capacity compared to traditional silane systems.

5. Conclusions

In conclusion, COOHSiT, a novel building block for functional silanization, offers three key advantages: a versatile carboxyl functional group, an intramolecular amide structure, and a stable tricyclic caged architecture. It operates reliably in both aqueous and anhydrous solvents, allowing for controlled silanization and the formation of thin, highly ordered, and uniform films on silicon substrates. Compared to similar carboxyl silane (COOHSi), COOHSiT coatings exhibit superior molecular homogeneity, morphology, hydrolytic stability, and functional group accessibility. Moreover, COOHSiT-based interfaces demonstrated efficient protein immobilization *via* EDC/NHS coupling in immunoassay experiments, confirming their robust performance in biosensing applications. Beyond enhancing the silatrane toolbox, COOHSiT paves the way for next-generation materials in biomedical diagnostics and environmental monitoring. Looking ahead, the future of silatrane chemistry involves the design and synthesis of structurally diverse silatranes tailored to the demands of nanostructure engineering and interface optimization.

Author contributions

Van-Truc Vu: conceptualization, formal analysis, investigation, methodology, visualization, writing – original draft; Pei-Yun Hsiao: formal analysis, investigation; Ting-Chou Chang: methodology, resources; Lai-Kwan Chau: conceptualization, methodology, supervision, funding acquisition, writing – original draft, writing – review and editing; Chun-Jen Huang: data curation, conceptualization, funding acquisition, project administration, supervision, validation, writing – review and editing.

Conflicts of interest

The authors declare that they have no conflicts of interest that could have appeared to influence the work reported in this paper.

Data availability

No additional datasets were generated or analyzed during the current study, and no public repository deposition is required.

All data generated or analyzed during this study are included in this published article and its supplementary information (SI) files. Supplementary information: figures of ^{1}H NMR characterization for COOHSiT and COOHSi; mass spectrum of COOHSiT; time-course NMR spectra of COOHSiT and COOHSi in MeOD containing 10% diH$_2$O; deconvolution of XPS C 1s and Si 2p peaks of wafers modified with COOHSiT and COOHSi in anhydrous and hydrated ethanol; deconvolution of XPS N 1s peaks of COOHSiT- and COOHSi-coated wafers after EDC/NHS activation; and tables of solubility profile of COOHSiT and COOHSi across different organic solvents; atomic% of COOHSiT- and COOHSi-modified wafers calculated by XPS; atomic% of COOH-terminated wafers after NHS activation calculated by XPS. See DOI: https://doi.org/10.1039/d5ma01020a.

Acknowledgements

References

1 F. Ahangaran and A. H. Navarchian, *Adv. Colloid Interface Sci.*, 2020, **286**, 102298.

2 L. Chen, S. Zhang, Y. Duan, X. Song, M. Chang, W. Feng and Y. Chen, *Chem. Soc. Rev.*, 2024, **53**, 1167–1315.

3 E. W. Colvin, *Chem. Soc. Rev.*, 1978, 7, 15–64.

4 A. Veloso, X. Cheng and K. Kerman, *Biosensors for medical applications*, Elsevier, 2012, pp. 3–40.

5 L. Wang, U. S. Schubert and S. Hoeppener, *Chem. Soc. Rev.*, 2021, **50**, 6507–6540.

6 K. Omae, T. Sakai, H. Sakurai, K. Yamazaki, T. Shibata, K. Mori, M. Kudo, H. Kanoh and M. Tati, *Arch. Toxicol.*, 1992, **66**, 750–753.

7 C. Haensch, S. Hoeppener and U. S. Schubert, *Chem. Soc. Rev.*, 2010, **39**, 2323–2334.

8 S. P. Pujari, L. Scheres, A. T. Marcelis and H. Zuilhof, *Angew. Chem., Int. Ed.*, 2014, **53**, 6322–6356.

9 J. L. Troiano, R. H. Crabtree and G. W. Brudvig, *ACS Appl. Mater. Interfaces*, 2022, **14**, 6582–6589.

10 A. Ulman, *Chem. Rev.*, 1996, **96**, 1533–1554.

11 A. N. Rider, D. R. Arnott and J. J. Mazza, *Aircraft Sustainment and Repair*, Elsevier, 2018, pp. 253–323.

12 S. Savard, L. P. Blanchard, J. Léonard and R. Prud'Homme, *Polym. Compos.*, 1984, **5**, 242–249.

13 M.-C. Brochier Salon and M. N. Belgacem, *Phosphorus, Sulfur Silicon Relat. Elem.*, 2011, **186**, 240–254.

14 C. M. Halliwell and A. E. Cass, *Anal. Chem.*, 2001, **73**, 2476–2483.

15 C.-J. Huang and Y.-Y. Zheng, *Langmuir*, 2018, **35**, 1662–1671.

16 M. V. Rivas, M. J. A. Muñetón, A. V. Bordoni, M. V. Lombardo, C. C. Spagnuolo and A. Wolosiuk, *J. Mater. Chem. B*, 2023, **11**, 1628–1653.

17 M.-C. B. Salon and M. N. Belgacem, *Colloids Surf., A*, 2010, **366**, 147–154.

18 A. Sáenz-Galindo, L. I. López-López, N. Fabiola, A. O. Castañeda-Facio, L. A. Rámirez-Mendoza, K. C. Córdova-Cisneros and D. de Loera-Carrera, *Carboxylic acid: Key role in life sciences*, 2018, vol. 35.

19 M. L. Bender, *Chem. Rev.*, 1960, **60**, 53–113.

20 J. D. Coyle, *Chem. Rev.*, 1978, **78**, 97–123.

21 T. A. H. Tran, V. T. Vu and C.-J. Huang, *Langmuir*, 2024, **40**, 24516–24527.

22 Y.-Y. Chen, K.-T. Huang and C.-J. Huang, *Dyes Pigm.*, 2025, **232**, 112488.

23 J.-Y. Chen, K.-T. Huang, S. Yau and C.-J. Huang, *Langmuir*, 2024, **40**, 13236–13246.

24 A. C. Rustan and C. A. Drevon, *Encyclopedia of life sciences*, 2005, vol. 1, pp. 1–7.

25 S. Sam, L. Touahir, J. Salvador Andresa, P. Allongue, J.-N. Chazalviel, A. Gouget-Laemmel, C. Henry de Villeneuve, A. Moraillon, F. Ozanam and N. Gabouze, *Langmuir*, 2010, **26**, 809–814.

26 M. J. Fischer, *Surface plasmon resonance: methods and protocols*, 2010, pp. 55–73.

27 M. D'Este, D. Eglin and M. Alini, *Carbohydr. Polym.*, 2014, **108**, 239–246.

28 A. Feinle, S. Flaig, M. Puchberger, U. Schubert and N. Hüsing, *Chem. Commun.*, 2015, **51**, 2339–2341.

29 Y. An, M. Chen, Q. Xue and W. Liu, *J. Colloid Interface Sci.*, 2007, **311**, 507–513.

30 S. E. Henkelis, S. J. Percival, L. J. Small, D. X. Rademacher and T. M. Nenoff, *Membranes*, 2021, **11**, 176.

31 S. N. Adamovich, E. N. Oborina, A. M. Nalibayeva and I. B. Rozentsveig, *Molecules*, 2022, **27**, 3549.

32 C.-T. Chiang, V. T. Vu, Y.-T. Cheng and C.-J. Huang, *ACS Appl. Mater. Interfaces*, 2023, **15**, 28524–28535.

33 S.-W. Chen, T. T. A. Hong, C.-T. Chiang, L.-K. Chau and C.-J. Huang, *J. Taiwan Inst. Chem. Eng.*, 2022, **132**, 104129.

34 J. Puri, R. Singh and V. K. Chahal, *Chem. Soc. Rev.*, 2011, **40**, 1791–1840.

35 K. L. Materna, J. Jiang, R. H. Crabtree and G. W. Brudvig, *ACS Appl. Mater. Interfaces*, 2018, **11**, 5602–5609.

36 M. J. Oh, I. Kownacki and M. Kubicki, *ACS Sustainable Chem. Eng.*, 2024, **12**, 2049–2057.

37 V. Pestunovich, S. Kirpichenko and M. Voronkov, *The chemistry of organic silicon compounds*, 1998, vol. 2, pp. 1447–1537.

38 T.-A. Chen, T. Yu, V. T. Vu, C.-J. Huang and C.-M. Chen, *ACS Appl. Nano Mater.*, 2024, **7**, 4874–4885.

39 Y. Peng, B. Chen, J. Li, X. Chen, X. Guo and D. Wang, *ChemElectroChem*, 2025, 2500182.

40 G. Singh, S. Gupta, J. D. Kaur, P. Markan, R. Yadav, R. Sehgal, J. Singh and R. Singh, *J. Mol. Struct.*, 2023, **1288**, 135687.

41 W. Charoenpinijkarn, M. Suwankruhasn, B. Kesapabutr, S. Wongkasemjit and A. M. Jamieson, *Eur. Polym. J.*, 2001, **37**, 1441–1448.

42 J. Andersson, J. Järlebark, S. Kk, A. Schaefer, R. Hailes, C. Palasingh, B. Santoso, V.-T. Vu, C.-J. Huang and F. Westerlund, *ACS Appl. Mater. Interfaces*, 2023, **15**, 10228–10239.

43 M. G. Voronkov, *Bioactive Organo-Silicon Compounds*, 2006, pp. 77–135.

44 M. A. Ramin, G. Le Bourdon, K. Heuze, M. Degueil, T. Buffeteau, B. Bennetau and L. Vellutini, *Langmuir*, 2015, **31**, 2783–2789.

45 Y.-S. Wang, S. Yau, L.-K. Chau, A. Mohamed and C.-J. Huang, *Langmuir*, 2018, **35**, 1652–1661.

46 H.-L. Liu, Y.-T. Tseng, M.-C. Lai and L.-K. Chau, *Biosensors*, 2022, **12**, 746.

47 L. S. Guthula, K.-T. Yeh, W.-L. Huang, C.-H. Chen, Y.-L. Chen, C.-J. Huang, L.-K. Chau, M. W. Chan and S.-H. Lin, *Biosens. Bioelectron.*, 2022, **214**, 114540.

48 C.-Y. Chiang, T.-T. Huang, C.-H. Wang, C.-J. Huang, T.-H. Tsai, S.-N. Yu, Y.-T. Chen, S.-W. Hong, C.-W. Hsu and T.-C. Chang, *Biosens. Bioelectron.*, 2020, **151**, 111871.

49 A. Chandrasekaran, R. O. Day and R. R. Holmes, *J. Am. Chem. Soc.*, 2000, **122**, 1066–1072.

50 R. Qi, D. L. Jones, Q. Liu, Q. Liu, Z. Li and C. Yan, *Polym. Test.*, 2021, **93**, 107009.

51 R. Vasudeva, S. Venkata, N. Venkateswarlu, B. Pushpalatha, B. Sukhendu and T. Vijaya, *Appl. Nanosci.*, 2015, **5**, 801–807.

52 M. Y. Bashouti, Y. Paska, S. R. Puniredd, T. Stelzner, S. Christiansen and H. Haick, *Phys. Chem. Chem. Phys.*, 2009, **11**, 3845–3848.

53 A. Dolgov, D. Lopaev, C. Lee, E. Zoethout, V. Medvedev, O. Yakushev and F. Bijkerk, *Appl. Surf. Sci.*, 2015, **353**, 708–713.

54 W. Skorupa and R. Yankov, *Mater. Chem. Phys.*, 1996, **44**, 101–143.

55 A. Ganguly, S. Sharma, P. Papakonstantinou and J. Hamilton, *J. Phys. Chem. C*, 2011, **115**, 17009–17019.

56 A. V. Ramya, R. Thomas and M. Balachandran, *Ultrason. Sonochem.*, 2021, **79**, 105767.

57 F. Ekiz, F. Oğuzkaya, M. Akin, S. Timur, C. Tanyeli and L. Toppare, *J. Mater. Chem.*, 2011, **21**, 12337–12343.

58 R. Jansen and H. Van Bekkum, *Carbon*, 1995, **33**, 1021–1027.

59 J. Bae, D. S. Kim, H. Yoo, E. Park, Y.-G. Lim, M.-S. Park, Y.-J. Kim and H. Kim, *ACS Appl. Mater. Interfaces*, 2016, **8**, 4541–4547.

60 G. Zheng, Y. Xiang, L. Xu, H. Luo, B. Wang, Y. Liu, X. Han, W. Zhao, S. Chen and H. Chen, *Adv. Energy Mater.*, 2018, **8**, 1801718.

61 V. Kankanala, M. Zubair and S. K. Mukkamalla, *Carcinoembryonic Antigen*, StatPearls, 2024.

62 C. I. Crucho, *Compounds*, 2023, **3**, 280–297.

63 K. L. Williamson and K. M. Masters, *Macroscale and microscale organic experiments*, Houghton Mifflin, Boston, 1999.

64 B. Zhuang, G. Ramanauskaite, Z. Y. Koa and Z.-G. Wang, *Sci. Adv.*, 2021, **7**, eabe7275.

65 L. M. Wancket, J. C. Schuh and E. Drevon-Gaillot, *Haschek and Rousseaux's Handbook of Toxicologic Pathology*, Elsevier, 2023, pp. 427–466.

66 C. Pavan, M. Delle Piane, M. Gullo, F. Filippi, B. Fubini, P. Hoet, C. J. Horwell, F. Huaux, D. Lison and C. Lo Giudice, *Part. Fibre Toxicol.*, 2019, **16**, 1–10.

67 D. Wu and A. I. Cederbaum, *J. Biol. Chem.*, 1996, **271**, 23914–23919.

68 S. Clave, X. Joya, J. Salat-Batlle, O. Garcia-Algar and O. Vall, *Toxicol. Lett.*, 2014, **225**, 216–221.

69 Y.-H. Deng, L.-H. Li, J. He, M. Li, Y. Zhang, X.-M. Wang, F.-Z. Cui and H. Xia, *Mol. Med. Rep.*, 2015, **11**, 975–981.

70 C. Ran, G. Ding, W. Liu, Y. Deng and W. Hou, *Langmuir*, 2008, **24**, 9952–9955.

71 Y. Ji, X. Yang, Z. Ji, L. Zhu, N. Ma, D. Chen, X. Jia, J. Tang and Y. Cao, *ACS Omega*, 2020, **5**, 8572–8578.

72 A. Johansson, P. Kollman, S. Rothenberg and J. McKelvey, *J. Am. Chem. Soc.*, 1974, **96**, 3794–3800.

73 S. N. Adamovich, A. M. Nalibayeva, Y. N. Abdikalykov, I. A. Ushakov, E. N. Oborina and I. B. Rozentsveig, *Int. J. Mol. Sci.*, 2023, **24**, 13818.